JOURNAL OF MAGNETIC RESONANCE **126,** 229–241 (1997)
ARTICLE NO. MN971160

X-Band Pulsed ENDOR Study of ^{57}Fe-Substituted Sodalite—The Effect of the Zero-Field Splitting

Rotem Vardi,* Marcelino Bernardo,† Hans Thomann,† Karl G. Strohmaier,†
David E. W. Vaughan,† and Daniella Goldfarb*

*Department of Chemical Physics, Weizmann Institute of Science, 76100 Rehovot, Israel; and †Exxon Research and Engineering Company, Route 22 East, Annandale, New Jersey 08801

Received November 25, 1996; revised March 6, 1997

X-band (~9.3 GHz) pulsed ENDOR measurements were carried out on ^{57}Fe-substituted sodalite (FeSOD) which contains only one type of Fe(III) ($S = \frac{5}{2}$) located at a framework site. The ENDOR spectrum recorded at $g = 2$ shows three doublets corresponding to the six M_S manifolds. The assignment of these signals was confirmed by hyperfine-selective and triple ENDOR experiments. The components of each of the doublets had different intensities, reflecting the different populations of the EPR energy levels at the measurement temperature, 1.8 K. ENDOR spectra were recorded at magnetic fields within the EPR powder pattern, and the field dependence observed showed an anisotropic behavior, unexpected from the isotropic character of the ^{57}Fe(III) hyperfine coupling. This dependence was attributed to the high-order effects of the zero-field splitting (ZFS) interaction on the ENDOR frequencies. Three different theoretical approaches were used to account for the dependence of the ENDOR spectrum on the ZFS interaction. The first involves the exact diagonalization of the total spin Hamiltonian, the second uses third-order perturbation approximations, and the third employs an effective nuclear Hamiltonian for each of the M_S manifolds. The simulations showed that the ENDOR signals of the $M_S = \pm 5/2$ ($\nu_{\pm 5/2}$) manifold are the least sensitive to the magnitude of the ZFS parameter D and are therefore the most appropriate for the determination of a_{iso}. It is shown that at X band and a_{iso} values of about 30 MHz, the perturbation approach is valid up to D values of 500 MHz if all three doublets are concerned. However, if only the $\nu_{\pm 5/2}$ doublet is considered, then this approach is valid for $D < 1000$ MHz. The third approach was found inappropriate for a_{iso} values of ~30 MHz. Using the method of exact diagonalization together with orientation selectivity, the trends observed in the experimental spectra could be reproduced. The ENDOR spectra of the ^{57}Fe-substituted zeolites ZSM5, L, and mazzite showed broad and ill-defined peaks since the ZFS of Fe(III) in these zeolites is significantly larger than that of FeSOD. Because this broadening is a high-order effect, it can be significantly reduced at higher spectrometer frequencies.

INTRODUCTION

The incorporation of iron into aluminosilicate and aluminophosphate molecular sieves has been a subject of numerous studies due to the potential new catalytic properties of the modified materials (*1–9*). In these Fe-substituted materials, the iron does not necessarily exclusively occupy framework sites. Fe cations can also be found at extra-framework sites, balancing the negative charge of the framework, or as an interstitial phase of small particles located either within the molecular sieve cavities or between the crystallites (*10–12*). In order to control and optimize the catalytic activity of the iron-substituted materials, it is necessary to know which type of iron is responsible for the activity, and therefore an unambiguous characterization of the various iron sites and types is essential.

One of the methods commonly applied to characterize Fe(III) sites in molecular sieves is EPR spectroscopy. EPR can provide information regarding the number of the different types of Fe(III) present (lower limit only), and it gives general information regarding their symmetry. However, because of its low resolution, arising from the inhomogeneous broadening caused by the zero-field splitting (ZFS) interaction, the EPR spectrum usually does not give detailed information on the local environment of the Fe(III) (*13*). Additional characterization information can be obtained from the NMR frequencies of ^{57}Fe(III) and of other nuclear spins coupled to the iron. These, in turn, give the corresponding hyperfine interactions which provide information such as the identity of neighboring atoms, the degree of covalency, and bonding distances. The NMR frequencies are best determined from electron–nuclear double-resonance (ENDOR) spectroscopy (*14, 15*) and/or electron spin-echo-envelope modulation (ESEEM) techniques (*16, 17*). Mössbauer spectroscopy can also provide the hyperfine interaction of ^{57}Fe(III) but ENDOR spectroscopy may be advantageous due to the additional resolution provided by the EPR spectrum and the broad scope of experiments offered by the pulsed methodology.

The hyperfine interaction of ^{57}Fe(III) (d^5, $S = \frac{5}{2}$, $I = \frac{1}{2}$) is predominately isotropic (*18*) and the ENDOR frequencies, given to second order, are (*15*)

1090-7807/97 $25.00

$$\nu(M_S)_{M_I \leftrightarrow M_{I+1}} = |-\nu_I + M_s a_{\text{iso}} - \frac{a_{\text{iso}}^2 M_S}{\nu_0}(M_I + M_S + \tfrac{1}{2})|, \quad [1]$$

where ν_0 and ν_I are the electronic and nuclear Larmor frequencies, respectively, and a_{iso} is the isotropic hyperfine constant. The first-order ^{57}Fe(III) ENDOR spectrum consists of three doublets, centered at $\frac{1}{2}a_{\text{iso}}$, $\frac{3}{2}a_{\text{iso}}$, and $\frac{5}{2}a_{\text{iso}}$, and each doublet is split by $2\nu_I$. The higher-order perturbation terms cause deviations of the splitting of the doublets from $2\nu_I$ (see Eq. [1]) and shift the center of the doublets (*19*).

The number of ^{57}Fe(III) ENDOR studies (CW or pulse) where the electron spin Zeeman interaction dominates ($g\beta H_0 \gg D$, and D is the ZFS parameter) and all five EPR transitions can be observed have been limited so far. The reported experimental results were mostly on single crystals (*20–22*) and the specific effects of the ZFS interaction on the ENDOR frequencies was not analyzed. Moreover, the characteristics of the orientation-selective spectra in orientationally disordered samples have not been addressed. It is expected that the ZFS interaction will introduce a significant inhomogeneous broadening in the ENDOR spectra (*19*).

In this work, we present a detailed X-band pulsed ENDOR study of ^{57}Fe-substituted sodalite (^{57}FeSOD), which contains only one type of Fe(III) with a relatively small D, located in a framework tetrahedral site (*13, 23*). Although the Zeeman and hyperfine interactions of high-spin ^{57}Fe(III) are highly isotropic (*18*), the ENDOR spectra showed significant orientation dependence. The orientation dependence is attributed to the ZFS interaction and is confirmed by simulations. Three different theoretical approaches were used in the simulations: (i) numerical diagonalization of the total spin Hamiltonian, (ii) third-order perturbation treatment of the ZFS and hyperfine interactions, and (iii) analytical diagonalization of nuclear Hamiltonians, each representing a different M_S manifold, employing an effective $\langle S_z \rangle$ value obtained by a third-order perturbation treatment of the ZFS interaction. It is found that for a hyperfine coupling constant of about 30 MHz, which is the typical value for high-spin ^{57}Fe(III), method (ii) is valid only for $D < 500$ MHz. The third method is not appropriate because the second-order effects of the hyperfine coupling are neglected.

EXPERIMENTAL

Sample preparation. The Fe-substituted zeolites were synthesized according to published procedures using an enriched $^{57}FeCl_3$ solution prepared by dissolving $^{57}Fe_2O_3$ in excess 1N HCl solution. The compositions of the zeolites studied, and the appropriate references for the synthesis procedures are listed in Table 1.

ENDOR measurements. The pulsed-ENDOR measurements were carried out at ≈9.34 GHz and 1.8 K on a homebuilt spectrometer described elsewhere (*26, 27*). ENDOR spectra were obtained using the Davies ENDOR sequence (*28*):

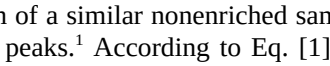

For signal assignment, the hyperfine-selective (HS) ENDOR sequence (*29*)

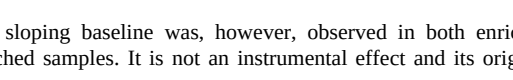

and the time-domain triple sequence (*30*)

were employed. In alternating scans, the phase of the echo-forming pulses was varied by 180°, reversing the sign of the echo and thereby eliminating baseline offsets. The length of the microwave (mw) pulses was 50, 30, 50 ns, respectively, and the width of the RF pulse was 2–3 μs. The repetition rate was 50 Hz for ^{57}FeSOD and 333 Hz for the other zeolites. For ^{57}FeSOD, strong echo modulations due to interactions with ^{27}Al and ^{23}Na were observed, and τ was chosen to coincide with the second maxima of the two-pulse ESEEM pattern (0.49–0.71 μs).

RESULTS

ENDOR Measurements

The EPR spectrum of ^{57}FeSOD at X band consists of a major singlet at $g = 2$ corresponding to the $|-\frac{1}{2}\rangle \rightarrow |\frac{1}{2}\rangle$ transition and two wings which are due to all the other EPR transitions (*13*). The ENDOR spectrum recorded at $g = 2.0$, shown in the bottom trace of Fig. 1, exhibits three groups of peaks with maxima at 15.4, 42.6, and 71.4 MHz and weaker shoulders at 14.3, 45.1, and 72.8 MHz. The ENDOR spectrum of a similar nonenriched sample did not show any of these peaks.[1] According to Eq. [1], the intense peaks at

[1] The sloping baseline was, however, observed in both enriched and nonenriched samples. It is not an instrumental effect and its origin is not clear.

TABLE 1
The Composition of the Zeolites Investigated, Given in Relative Atom Ratios

Sample	Zeolite	*T* sites	Fe	Al	Si	Na	K	$\frac{\text{Fe}}{\text{Fe + Al + Si}}$ [a]	Ref.[b]
^{57}FeSOD	Sodalite	1	0.001	0.999	0.96	1.32		0.05	(*7*)
^{57}FeLTL	Linde L	2	0.002	0.998	2.71		1.01	0.07	(*6*)
^{57}FeMAZ	Mazzite	2	0.003	0.997	2.92	0.78		0.07	(*24*)
^{57}FeMFI	ZSM5	12	0.0018	0.982	28.2	0.65		0.06	(*25*)

[a] Molar ratio of Fe expressed as a molar percent.
[b] Synthesized according to these references.

42.6 and 71.4 MHz were assigned to the $M_S = -\frac{3}{2}$ and $-\frac{5}{2}$ manifolds ($\nu_{-3/2}$ and $\nu_{-5/2}$), respectively, whereas their shoulders were assigned to the $M_S = \frac{3}{2}$ and $\frac{5}{2}$ manifolds ($\nu_{3/2}$ and $\nu_{5/2}$) (*31*). The assignment was based on the intensity difference within the $\nu_{\pm 3/2}$ and $\nu_{\pm 5/2}$ doublets attributed to different populations of the energy levels at low temperatures (1.8K) (*32*). The ENDOR signals at 14.3 and 15.4 MHz were assigned to the $M_S = \pm\frac{1}{2}$ manifolds ($\nu_{\pm 1/2}$). Using these values and the first-order approximation for the hyperfine frequencies (Eq. [1]), three different values, −30.8, −27.7, and −28.6 MHz, were obtained for a_{iso}. This variation in a_{iso} and the different splittings of the three doublets could not be accounted for by adding the second-order contribution of the hyperfine interaction (see Eq. [1]).

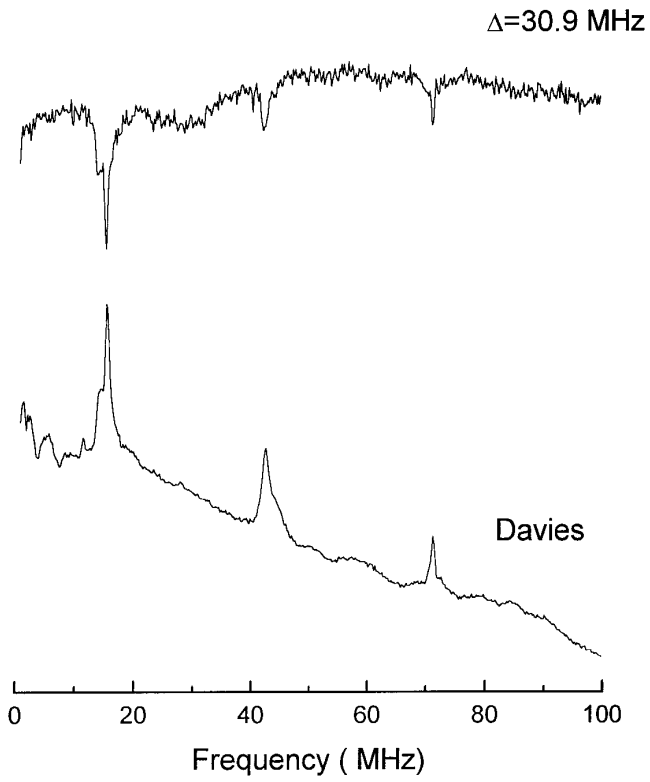

FIG. 1. Davies ENDOR (bottom) and HS-ENDOR with $\Delta = 30.9$ MHz (top) spectra of ^{57}FeSOD spectra recorded at $H_0 = 3326$ G ($g = 2.0$) and $t_{rf} = 2.0$ μs T = 4.0 μs and $\tau = 0.56$ μs.

To confirm that these peaks indeed arise from a single Fe(III) site, a HS-ENDOR experiment was carried out. This experiment correlates all ENDOR transitions originating from a hyperfine coupling preselected by $\Delta = \omega_{mw1} - \omega_{mw2} = a_{iso}$, where ω_{mw1} is the frequency of the selective π pulse and ω_{mw2} is the frequency of the echo-forming pulses (*29*). The spectrum recorded with $\Delta = 30.9$ MHz, shown at the top of Fig. 1, exhibits all the lines observed in the Davies ENDOR spectrum, in opposite phase, as expected. A triple experiment was also carried out to verify the assignment of the signals. In this experiment, one of the RF pulses is set to one of the ENDOR frequencies while the frequency of the other RF pulse is swept. This experiment selects only ENDOR transitions that have a common EPR energy level with the ENDOR transition excited by the fixed RF frequency (*14, 30*). For instance, if the RF is set to $\nu_{-5/2}$, $\nu_{-3/2}$ is expected to appear, whereas setting it to $\nu_{-3/2}$ should result in the appearance of $\nu_{-5/2}$ and $\nu_{-1/2}$. The triple experiment was carried out at $H_0 = 3025$ G ($g = 2.19$), where the $\nu_{\pm 3/2}$ peaks are well resolved but the $\nu_{\pm 1/2}$ peaks are very weak (see top of Fig. 2) as this field is outside the range of the $|-\frac{1}{2}\rangle \rightarrow |\frac{1}{2}\rangle$ EPR transition. The triple spectra obtained are shown in Fig. 2. These spectra confirm the assignment of the 42.3 and 71.4 MHz peaks to the $M_S = -\frac{3}{2}$ and $-\frac{5}{2}$ manifolds, respectively.

A series of orientation-selective pulsed-ENDOR spectra which were recorded across the EPR powder pattern are presented in Fig. 3. The $\nu_{\pm 1/2}$ signals appear in the narrowest range of fields as compared to the other two doublets. This is expected if one considers the simulated powder patterns of the individual EPR transitions shown in Fig. 4. All transitions contribute to the center of the spectrum (positions A in Figs. 4a, 4b); however, as the edges of the spectrum are approached, the relative contribution of the $|-\frac{1}{2}\rangle \rightarrow |\frac{1}{2}\rangle$ transition decreases (positions B, C in Fig. 4). This leads to a significant reduction in the intensity of the $\nu_{\pm 1/2}$ signals. At

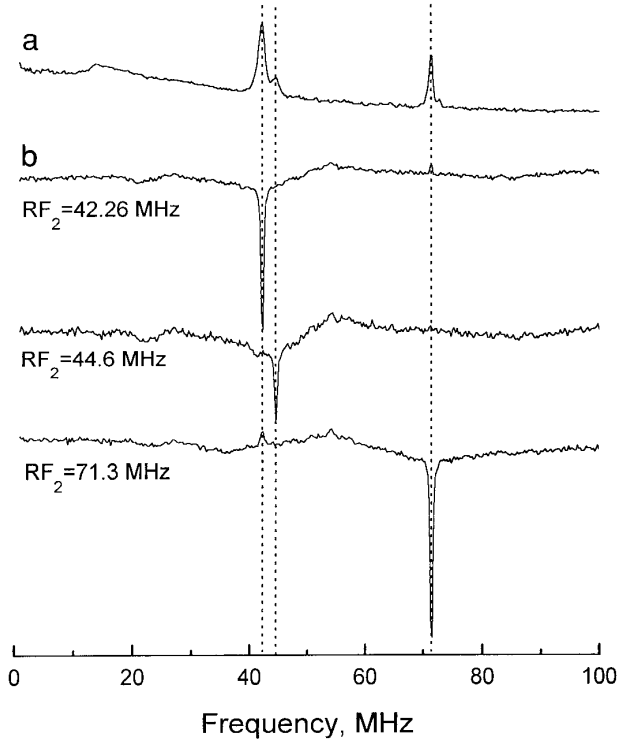

FIG. 2. (a) Davies ENDOR spectrum of ^{57}FeSOD and (b) triple spectra recorded with RF_2 frequencies as noted on the figure. In all spectra, H_0 = 3025 G, τ = 0.45 μs, and t_{RF} = 2.0 μs. The delay between the RF pulses was 0.1 μs. The vertical dotted lines were added to facilitate the observation of the peak positions.

the outer most edges, only the $|-\frac{5}{2}\rangle \rightarrow |-\frac{3}{2}\rangle$ and $|\frac{3}{2}\rangle \rightarrow |\frac{5}{2}\rangle$ transitions contribute, and therefore only $\nu_{\pm 3/2}$ and $\nu_{\pm 5/2}$ are observed. Other orientation-dependent effects are the field dependence of $\nu_{\pm 1/2}$ and $\nu_{\pm 3/2}$, which cannot be accounted for by the above considerations and/or by the expected variation in ν_I. We attribute this orientation dependence to the ZFS interaction which introduces anisotropy into the ENDOR frequencies as shown explicitly in the next section.

Theory and Simulations

Theoretical background. The spin Hamiltonian of high-spin ^{57}Fe(III) ($S = \frac{5}{2}$, $I = \frac{1}{2}$) is (*33*)

$$H = \nu_0 \hat{S}_z + A\left[\hat{S}_z^2 - \frac{1}{3}S(S+1)\right] + B_+(\hat{S}_+\hat{S}_z + \hat{S}_z\hat{S}_+) + B_-(\hat{S}_-\hat{S}_z + \hat{S}_z\hat{S}_-) + C_+\hat{S}_+^2 + C_-\hat{S}_-^2 + a_{iso}\hat{S}_z\hat{I}_z + \frac{a_{iso}}{2}(\hat{S}_+\hat{I}_- + \hat{S}_-\hat{I}_+) - \nu_I\hat{I}_z, \quad [2]$$

where

$$A = D\left[\left(\frac{3\cos^2\theta - 1}{2}\right) + \frac{3}{2}\eta\sin^2\theta\cos 2\phi\right], \eta = E/D, \quad [3]$$

$$B_\pm = \frac{D}{4}(-\sin 2\theta + \eta\sin 2\theta\cos 2\phi \pm i2\eta\sin\theta\sin 2\phi) \quad [4]$$

$$C_\pm = \frac{D}{4}[\sin^2\theta + \eta(\cos^2\theta + 1)\cos 2\phi \pm i2\eta\cos\theta\sin 2\phi] \quad [5]$$

and θ and ϕ give the direction of the magnetic field with respect to the principal axis system of the ZFS tensor, ν_0 =

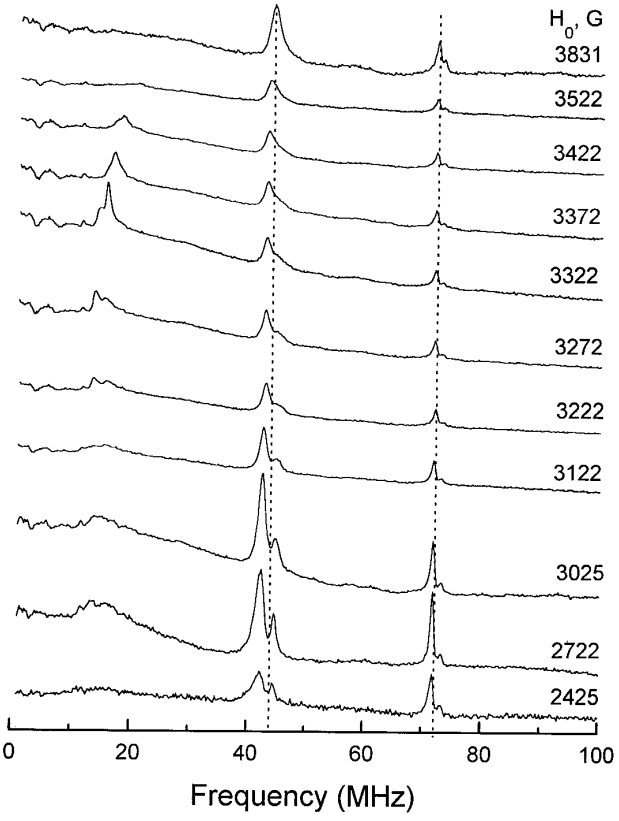

FIG. 3. Pulsed-ENDOR spectra of ^{57}FeSOD measured at different magnetic fields within the EPR powder pattern. The experimental parameters are as described in the legend to Fig. 1, and τ was in the range of 0.49–0.71 μs, depending on the field. The vertical dotted lines were added to facilitate the observation of the field dependence. The scale of the spectra recorded at 2425, 2722, and 3025 G was multiplied by a factor of 6.3 and that of 3122 and 3831 G by 1.41 and 4.41, respectively.

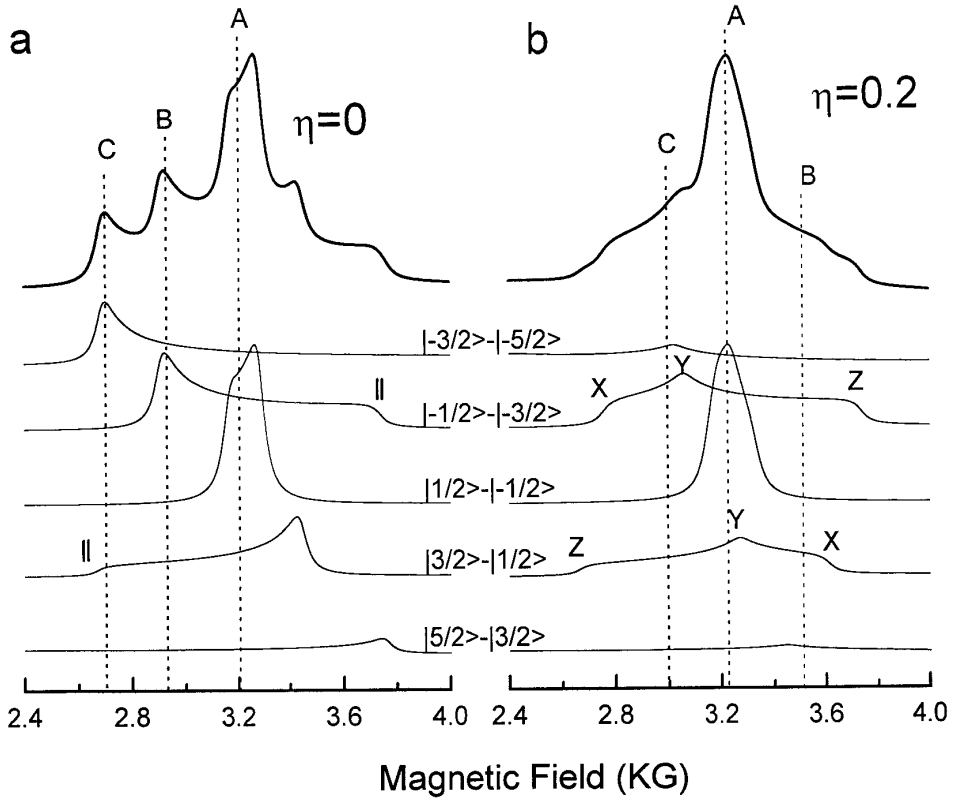

FIG. 4. Simulated absorption EPR powder patterns decomposed according to the various allowed transitions. The upper trace is the sum of all EPR transitions. The different Boltzmann populations at 1.8 K were taken into account. The parameters used in the simulations were $D = 750$ MHz, $a_{iso} = -28.8$ MHz and (a) $\eta = 0$ and (b) $\eta = 0.2$.

$g\beta H_0/h$ and $\nu_I = g_N\beta_N H_0/h$. Three different approaches were used to calculate the ENDOR frequencies. The first used numerical diagonalization of H and is referred to as the exact solution. In the second approach, third-order perturbation theory was employed. Using the energies corrected to third order, as given in (*33*), the following allowed ENDOR frequencies ($\Delta M_S = 0$ and $\Delta M_I = \pm 1$) were obtained:

where

$$S^{\pm}_{M_S} = S(S+1) - M_S(M_S \pm 1)$$

$$I^{\pm}_{M_I} = I(I+1) - M_I(M_I \pm 1).$$

The numbers in parentheses correspond to the order of the correction.

$$\nu^{\mathrm{ENDOR}(1)}_{M_S,M_I} = a_{\mathrm{iso}}M_S - \nu_I \qquad [6]$$

$$\nu^{\mathrm{ENDOR}(2)}_{M_S,M_I} = \frac{a^2_{\mathrm{iso}}}{\nu_0}\left[-S(S+1) + M_S^2 - M_S(2M_I - 1)\right] \qquad [7]$$

$$\begin{aligned}\nu^{\mathrm{ENDOR}(3)}_{M_S,M_I} = {} & \frac{a^3_{\mathrm{iso}}}{4\nu_0^2}\left[(-M_S + M_I - 1)S^+_{M_S}I^-_{M_I} + (M_S - M_I + 2)S^+_{M_S}I^-_{M_I-1}\right. \\ & \left. +(M_S - M_I - 1)S^-_{M_S}I^+_{M_I} - (M_S - M_I)S^-_{M_S}I^+_{M_I-1}\right] \\ & +\frac{2a_{\mathrm{iso}}B_+B_-}{\nu_0^2}\frac{1}{M_S}\left\{[S(S+1) - M_S^2]^2 - M_S^2\right\} + \frac{a_{\mathrm{iso}}C_+C_-}{2\nu_0^2}\left(S^+_{M_S}S^+_{M_S+1} - S^-_{M_S}S^-_{M_S-1}\right) \\ & +\frac{a^2_{\mathrm{iso}}A}{4\nu_0^2}\left[(2M_S + 1)S^+_{M_S}(I^-_{M_I} - I^-_{M_I-1}) - (2M_S - 1)S^-_{M_S}(I^+_{M_I} - I^+_{M_I-1})\right],\end{aligned} \qquad [8]$$

The third approach is similar to that developed by Mims to calculate the echo intensity in the two- and three-pulse ESEEM experiments (*34*), and in the following it will be referred to as the effective-nuclear-Hamiltonian (ENH) method. This approach was used by Larsen *et al.* (*35*) in the analysis of the ESEEM spectra of a $S = \frac{5}{2}$, $I = \frac{1}{2}$ system where the electronic–nuclear spin system was treated as a set of noninteracting two level systems. In this approach, a nuclear Hamiltonian is defined for each electronic M_S manifold, and the modulation frequencies are calculated using the eigenvalues of these Hamiltonians. This approximation is valid when the mw pulse-excitation bandwidth is very small compared to the ZFS interaction. For each of the M_S manifolds, an effective spin $\langle S_z \rangle$ was defined, neglecting any mixing due to the ZFS. In the present work, such mixing is taken into account as described below. A similar approach was employed by Coffino *et al.* (*36*) in the calculation of the ESEEM frequencies of a Mn^{2+} ($S = \frac{5}{2}$) system with small ZFS. There, however, all the nonsecular terms involving $\hat{S}_{x,y}$ were neglected in the calculation of the ESEEM frequencies and intensities but they were retained in the calculations of the EPR transitions contributing to the echo intensity. In our approach, $\hat{I}_{x,y,z}\hat{S}_{x,y}$ terms were neglected but terms with $\hat{S}_{x,y}$ were retained.

The Hamiltonian in Eq. [2] can be decomposed according to

$$H = H_S - \nu_I \hat{I}_z + \hat{\mathbf{S}} \cdot \mathbf{A} \cdot \hat{\mathbf{I}}, \qquad [9]$$

where H_S contains only pure electron spin terms such as the electron Zeeman interaction and the ZFS term. In Eq. [9], the hyperfine interaction is expressed in its general form. Assuming that $\mathbf{A}$ is too small to cause any significant mixing of the electronic spin states ($\nu_I \hat{I}_z$, $a_{\text{iso}}\hat{\mathbf{S}} \cdot \hat{\mathbf{I}} \ll H_S$), H can be expressed in a block diagonal form with a total of $2S + 1$ blocks, each corresponding to a $(2I + 1) \times (2I + 1)$ nuclear Hamiltonian. The representation of H in a block diagonal form requires the diagonalization of H_S using the transformation:

$$\mathbf{U}_S^{-1} H_S \mathbf{U}_S = H_S^D. \qquad [10]$$

The same transformation is then applied to the hyperfine interaction term which, after neglecting the off-diagonal terms involving $\hat{I}_{x,y,z}\hat{S}'_{x,y}$, becomes

$$\hat{\mathbf{S}}' \cdot \mathbf{A} \cdot \hat{\mathbf{I}} = A_{xz}\hat{I}_x\hat{S}'_z + A_{yz}\hat{I}_y\hat{S}'_z + A_{zz}\hat{I}_z\hat{S}'_z \qquad [11]$$

The prime indicates the new representation. Finally, each block in the block diagonal matrix corresponds to an effective nuclear Hamiltonian, H_{M_S}, given by

$$H_{M_S} = A'_{xz,M_S}\hat{I}_x + A'_{yz,M_S}\hat{I}_y + A'_{zz,M_S}\hat{I}_z - \nu_I \hat{I}_z, \qquad [12]$$

where $A'_{ij,M_S} = {}'\langle M_S | \hat{S}'_z | M_S \rangle' A_{ij} = \langle S'_z \rangle_{M_S} A_{ij}$ and the $|M_S\rangle'$ are the eigenvectors of H_S. The effective $\langle S'_z \rangle_{M_S}$ for each manifold can be obtained from the third-order-corrected eigenvectors (see Appendix). For a $S = \frac{5}{2}$, $I = \frac{1}{2}$ system, the block-diagonal matrix consists of six 2×2 blocks of the form:

$$H_{M_S} = \frac{1}{2}\begin{bmatrix} -\nu_I + \langle S'_z \rangle_{M_S} A_{zz} & \langle S'_z \rangle_{M_S}(A_{xz} - iA_{yz}) \\ \langle S'_z \rangle_{M_S}(A_{xz} + iA_{yz}) & \nu_I - \langle S'_z \rangle_{M_S} A_{zz} \end{bmatrix}. \qquad [13]$$

Diagonalization of H_{M_S} gives the ENDOR frequencies within each M_S manifold:

$$\nu_{M_S}^{\text{ENDOR}} = [(\langle S'_z \rangle_{M_S} A_{zz} - \nu_I)^2 - \langle S'_z \rangle_{M_S}^2 (A_{xz}^2 + A_{yz}^2)]^{1/2}. \qquad [14]$$

For an isotropic hyperfine interaction, as in ^{57}Fe(III), H_{M_S} is diagonal and the ENDOR frequencies become

$$\nu_{M_S}^{\text{ENDOR}} = |-\nu_I + a_{\text{iso}} \langle S'_z \rangle_{M_S}|. \qquad [15]$$

Neglecting the hyperfine enhancement factor and the different nutation frequencies of the various EPR transitions (*32*), we assumed that the intensity of a particular ENDOR transition is proportional to the intensity of the corresponding EPR transition, given by $W_{n \leftrightarrow m} = |\langle n | \hat{S}_x | m \rangle|^2$ (*37*). The different nutation frequencies of the EPR transitions were taken into account in the ESEEM simulations of a Mn^{2+} coupled to a $I = \frac{1}{2}$ nucleus carried out by Coffino *et al.* (*36*). At very low temperatures, the relative population of the energy levels, given by the Boltzmann factor, must be taken into account and the amplitude of the EPR signal is then described by (*32*)

$$I_{n \leftrightarrow m}^{\text{EPR}} \propto \frac{\exp[-(E_{|n\rangle} - E_{|m\rangle})/KT]}{\sum_{i=1}^{2S+1} \exp(-E_{|i\rangle}/KT)} \times W_{n \leftrightarrow m}. \qquad [16]$$

The intensities of the ENDOR signals are therefore

$$I_{n' \leftrightarrow n''}^{\text{ENDOR}} \propto I_{n \leftrightarrow m}^{\text{EPR}} \delta(n', n'' \pm 1). \qquad [17]$$

where the selection rule $\Delta M_I = \pm 1$ was applied and the n' and n'' levels are sublevels within the EPR n or m manifolds. In the above, only the allowed EPR transitions were considered.

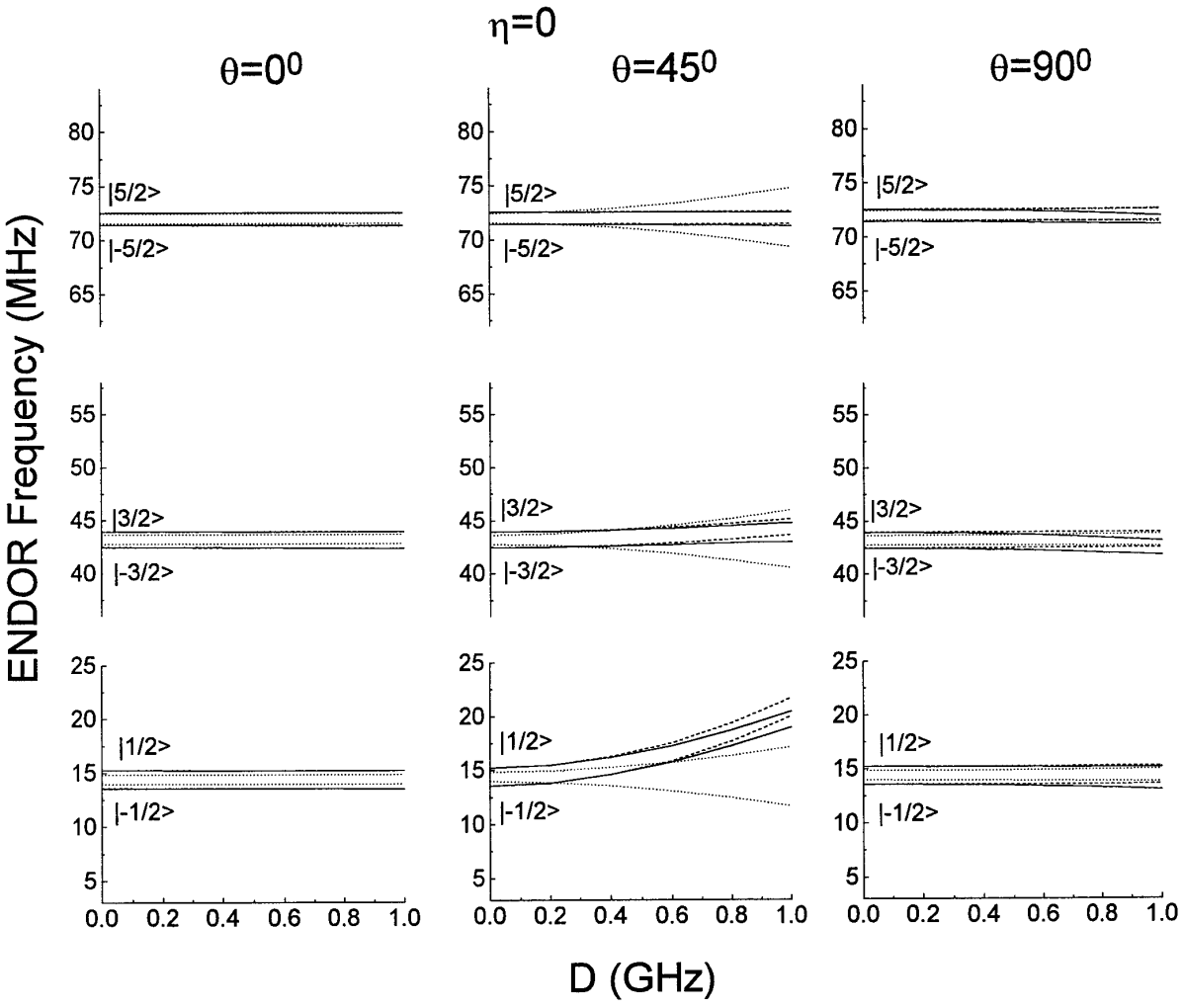

FIG. 5. Calculated ^{57}Fe ENDOR frequencies with $a_{iso} = -28.8$ MHz as a function of D ($\eta = 0$) for three different orientations, $\theta = 0°$, 45°, and 90° ($H_0 = 3200$ G). Three methods were used for the calculations, exact diagonalization (solid lines), third-order perturbation (dashed lines), and the effective-nuclear-Hamiltonian method (dotted line).

Simulations. Figure 5 shows the dependence of the ENDOR frequencies on D ($\eta = 0$) for $a_{iso} = -28.8$ MHz and three different θ values, 0°, 45°, and 90°, calculated using the three approaches described above. The range of D that was explored was limited to 1000 MHz which, according to the EPR spectrum, is an upper limit to the D value in FeSOD. For $\theta = 0°$, there is practically no difference between the exact diagonalization and the perturbation method because this H_S is diagonal (see Eq. [2]), and the ENDOR frequencies are independent of D. The splitting of the ν_{M_S} doublets is $|M_S|$-dependent due to the second-order effect of the hyperfine coupling (see Eq. [7]). While this dependence is clear in the curves obtained using the first two methods, it does not appear in the curves calculated with the ENH method. This is due to the elimination of the off-diagonal elements arising from the term $a_{iso}/2\ (\hat{S}_x\hat{I}_x + \hat{S}_y\hat{I}_y)$ which is responsible for the second-order hyperfine shift. The elimination of these terms is also responsible for the significantly difference behavior observed by the ENH method for $\theta = 45°$ and 90°.

The strongest dependence of the ^{57}Fe ENDOR frequencies on D is obtained when $\theta = 45°$, and it increases according to $\nu_{\pm 1/2} > \nu_{\pm 3/2} > \nu_{\pm 5/2}$. As D is raised, the $\nu_{\pm 1/2}$ doublet is shifted more toward the $\nu_{\pm 3/2}$ doublet and the $\nu_{\pm 3/2}$ doublet toward the $\nu_{\pm 5/2}$ doublet, though to a lesser extent. A comparison of the curves obtained from the three methods shows that the ENH approach is not appropriate for calculating the ENDOR frequencies when relatively large a_{iso} values are involved. The third-order perturbation method is suitable for values of D up to ~500 MHz if all ENDOR transitions are concerned. However, if only the $\nu_{\pm 5/2}$ doublet is considered, then the third-order perturbation approach is valid even for

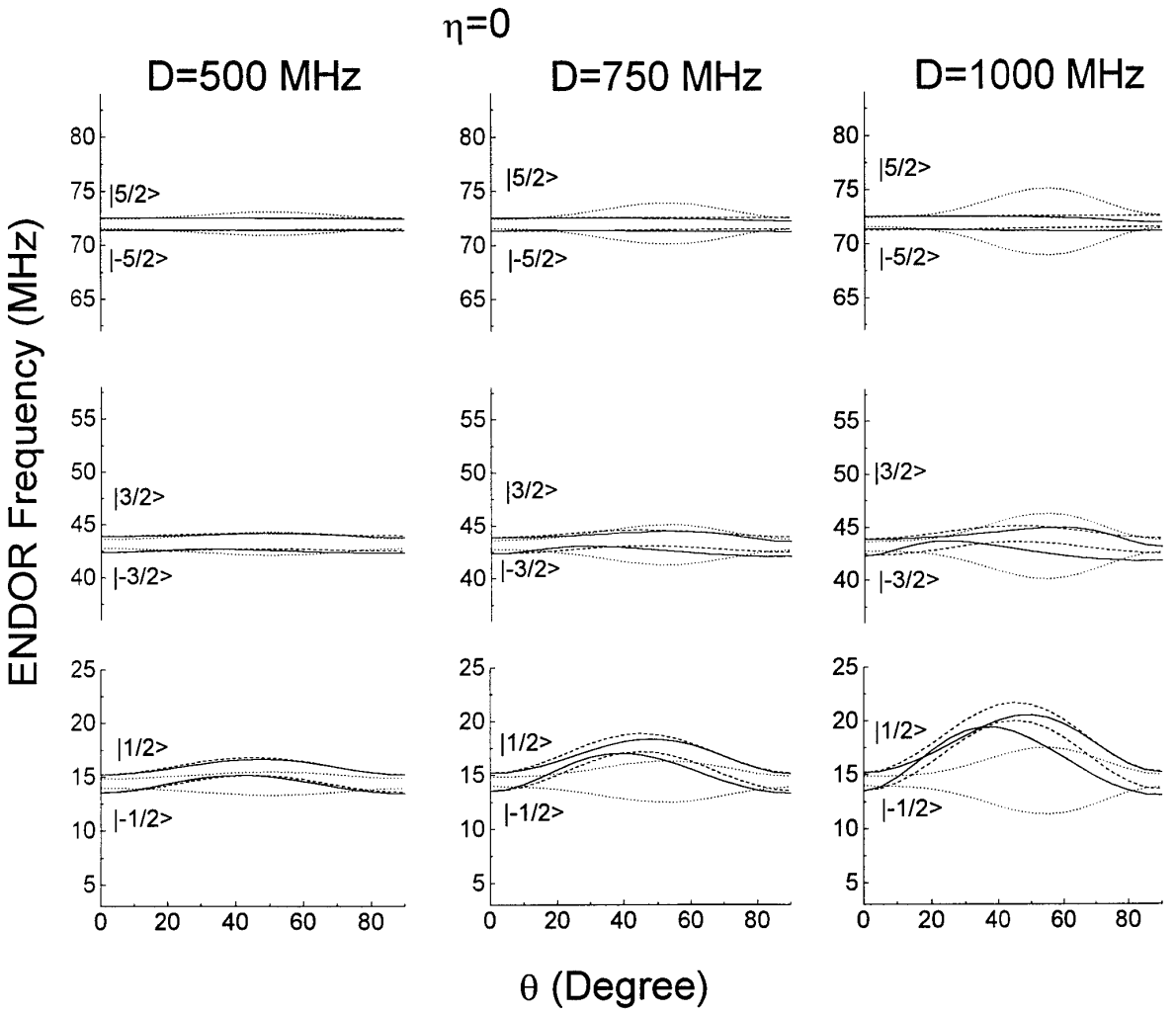

FIG. 6. The angular dependence of ^{57}Fe ENDOR frequencies calculated for $a_{iso} = -28.8$ MHz $D = 500$, 750, and 1000 MHz and $\eta = 0$ ($H_0 = 3200$ G). Three methods were used for the calculations, exact diagonalization (solid lines), third-order perturbation (dashed lines), and the effective-nuclear-Hamiltonian method (dotted line).

$D \sim 1000$ MHz. Calculations carried out with $\eta = 0.2$ showed the same general trend, though the detailed dependence was somewhat different. The angular dependence of the ^{57}Fe ENDOR frequencies for D values of 500, 750, and 1000 MHz and $\eta = 0$ is shown in Fig. 6. Again, the frequencies were calculated using the three different approaches presented above. The frequency span of each ENDOR frequency increases as follows, $\nu_{\pm 1/2} > \nu_{\pm 3/2} > \nu_{\pm 5/2}$, and the broadest powder pattern is expected for the $\nu_{\pm 1/2}$ doublet. This is in a good agreement with the experimental ENDOR spectra shown in Fig. 3.

This orientation dependence is expected once Eq. [8] is inspected. There are three terms which depend on the magnitude of the ZFS through $a_{iso}^2 A$, $a_{iso} B_+ B_-$ and $a_{iso} C_+ C_-$ and which depend on the M_S value. Figure 6 shows that the curves corresponding to $\nu_{\pm 1/2}$, obtained by the exact method, are to a good extent parallel for $D = 500$ MHz, but for the higher D values, strong deviations are clear. Similar trends were observed for a nonaxial ZFS tensor. Figure 6 also shows that the perturbation method is valid up to $D \sim 500$ MHz, and that for higher D values, the deviations are mainly related to the loss of symmetry with respect to $|M_S|$.

In order to simulate the orientation dependence of the ENDOR spectra shown in Fig. 3, the relative contribution of each of the EPR transitions excited by the mw pulse at the particular magnetic field at which the experiment has been carried must be determined. For each EPR transition, Fe centers with different orientations contribute to the signal and these must be determined as well. This requires the knowledge of D and E, which in turn can be obtained from simulations of the EPR spectrum. Simulations of the X- and W-band EPR spectra of ^{57}FeSOD gave $D = 750$ MHz and

$\eta \sim 0.2$ (*23, 38*). Using these values, a table was generated consisting of the resonant magnetic field, the EPR transitions that obey the resonance condition at this particular field, the corresponding orientation of the ZFS (θ and ϕ values), and the relative intensities of the EPR transition. When the perturbation theory method was applied, the resonant magnetic fields of each of the five EPR transitions at a particular orientation were calculated using the expressions for the EPR transitions given in Ref. (*33*). If the calculated field was within $\pm\Delta H$ from the field at which the ENDOR experiment was carried out, the orientation was added to the table. The width ΔH accounts for the inhomogeneous linewidth and the pulse spectral width. In the case of the exact solution, where the determination of the resonant field is not straight forward and long computation times are required (*37*), a different approach was adapted. The frequencies of the EPR transitions at all possible orientations were calculated using the magnetic field at which the experiment was performed, and when the frequencies were found to be within $\pm\Delta\nu$ from the spectrometer frequency, ν_0, the orientations were added to the table. The width $\pm\Delta\nu$ serves the same purpose as ΔH. A similar approach was employed by Coffino *et al.* (*36*).

The ENDOR spectra were calculated by summing over all transitions and orientations (listed in the table) that contribute to the EPR signal at a particular field, including the allowed width, ΔH or $\Delta\nu$. Each ENDOR frequency was convoluted with a Lorentzian lineshape with a width of 0.4 MHz. The major experimental features that we tried to reproduce in the simulations were: (i) the practical field independence of $\nu_{\pm 5/2}$, (ii) the frequency shift and lineshape of the $\nu_{\pm 3/2}$ peaks, and (iii) the field range at which each of the ENDOR signal appears. The simulated spectra shown in Figs. 7–9 were normalized independently, and therefore the absolute intensities of the various spectra are not comparable.

Figure 7 shows a series of orientation-selective ENDOR spectra calculated with $D = 750$ MHz, $\eta = 0.2$, and $a_{\text{iso}} = -28.8$ MHz. At 2425 G, of the $\nu_{\pm 5/2}$ only the $\nu_{5/2}$ component appears, whereas in the experimental spectra both are apparent (see Fig. 3). Increasing η to 0.3 gives better agreement with the experimental results as shown in Fig. 8. It represents the best-fit spectra we obtained, taking into account the constraints we had on D and E/D from the EPR spectrum. In general, the range of magnetic fields at which both $\nu_{\pm 5/2}$ are observed is determined by E/D and the total field range where $\nu_{5/2}$ or $\nu_{-5/2}$ appears depends on D. In the simulated spectra shown in Fig. 8, the field independence of $\nu_{\pm 5/2}$ is reproduced and the two methods of calculations give the same peaks as expected. The general field dependence of $\nu_{\pm 3/2}$ is reproduced as well; at low fields, the two signals are resolved, and as the field increases, more features appear. At the high-field

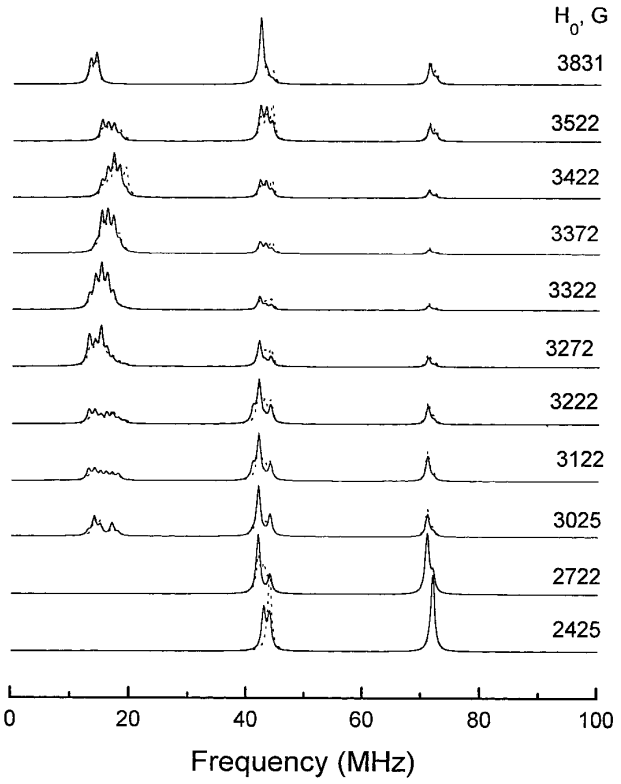

FIG. 7. Simulated orientation-selective ENDOR spectra calculated with $a_{\text{iso}} = -28.8$ MHz, $D = 750$ MHz, $\eta = 0.2$, $\Delta H = 15$ G, and $\Delta\nu = 0.1$ GHz. Spectra obtained using the exact calculation appear in solid lines whereas those obtained using the perturbation method are represented by dotted lines.

end of the series, the doublet merges into one signal, again in agreement with the experimental data. The general behavior of the $\nu_{\pm 1/2}$ signals in the range 3025–3522 G, in terms of width and frequency position, is also similar to experimental results, though the detailed lineshape of the signals is not reproduced. Furthermore, the relative intensities of the $\nu_{\pm 1/2}$ peaks in the calculated spectra are larger than in the experimental spectra, particularly at the high-field end. We attribute the discrepancies between the calculated and experimental spectra to the difficulties in determining accurately the relative contributions of the EPR transitions and the corresponding selected orientations to the echo at each field. This stems from neglecting the different nutation frequencies of the individual EPR transitions and from the large inhomogeneous linewidths which may include distributions in D and E. The value that was taken into account for the inhomogeneous linewidth was 15 G (or 0.1 GHz) which is most probably too small to adequately account for the experimental results.

When D increases further, the ENDOR peaks becomes significantly broader as shown in Fig. 9. If one takes into account large inhomogeneous broadening due to distribu-

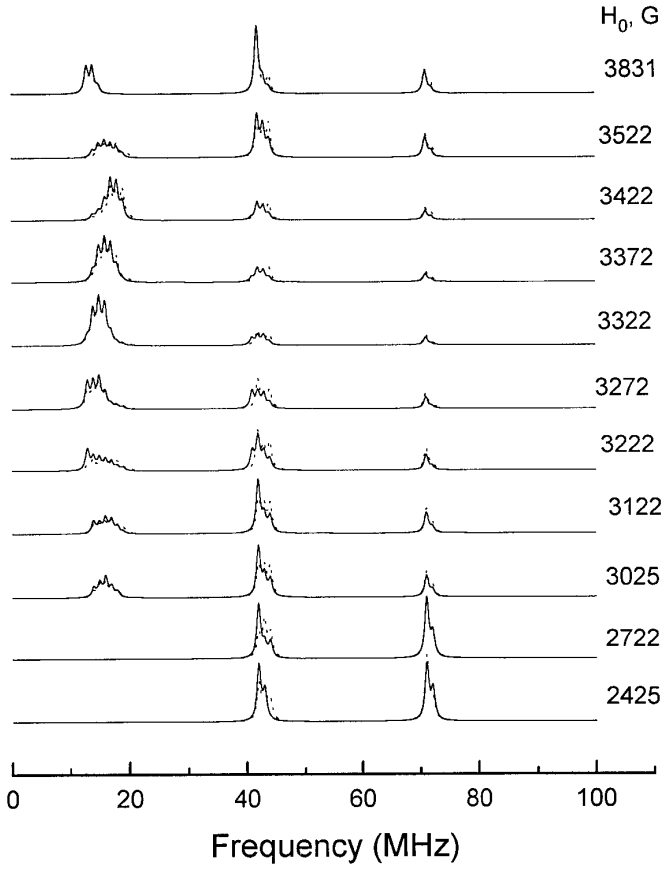

FIG. 8. Simulated orientation-selective ENDOR spectra calculated with $a_{iso} = -28.8$ MHz, $D = 750$ MHz, $\eta = 0.3$, $\Delta H = 15$ G, and $\Delta\nu = 0.1$ GHz. Spectra obtained using the exact calculation appear in solid lines, whereas those obtained using the perturbation method are represented by dotted lines.

tions in D and E, then for $D = 1500$ MHz the observation of the $\nu_{\pm 1/2}$ would be very difficult and most probably only the $\nu_{\pm 5/2}$ peaks can be observed. This was the case for the ENDOR spectra of ^{57}FeLTL, ^{57}FeMFI, and ^{57}FeMAZ presented in Fig. 10. The EPR peak of these zeolites at $g = 2$ is significantly broader than that of FeSOD (*13*). Only when the spectra were recorded at the high-field edge of the EPR spectrum (5000 G) could reasonable signals be observed. All three spectra show a broad signal at ~72 MHz which is assigned to $\nu_{\pm 5/2}$ and a broad feature around 51 MHz attributed to $\nu_{\pm 3/2}$. In these materials, the ZFS of the Fe(III) is significantly larger than in FeSOD (*23*).

DISCUSSION

It has been shown that in systems with a dominating electron Zeeman interaction and appreciable ZFS interaction the ZFS term introduces a significant inhomogeneous broadening in the ENDOR spectrum. The mechanism leading to this broadening is the same as that causing the appearance of forbidden EPR transitions ($\Delta M_s = \pm 1$, $\Delta M_I = \pm 1$) in the EPR spectra of Mn^{2+} (when $g\beta H_0 > D$) (*33*). The broadening is on the order of $a_{iso}D^2/\nu_0^2$ and therefore at X band (~9 GHz), values of $D > 1500$ MHz already broaden the ENDOR spectrum beyond detection. This effect can be significantly reduced at high fields as we have recently demonstrated by pulsed ENDOR measurements at 95 GHz carried out on the same zeolites studied in this work (*23*). At this frequency, the orientation-selective spectra of ^{57}FeSOD showed no orientation dependence, and the value obtained for a_{iso} (−29.0 MHz) was very close to the value determined from the X-band data and the simulations (−28.8 MHz). Moreover, the ENDOR signals of the other zeolites could be observed, thus confirming the analysis presented in this work.

When D is not too large and ENDOR spectra can be observed, the orientation dependence of the amplitudes of the various ENDOR peaks can provide information on the

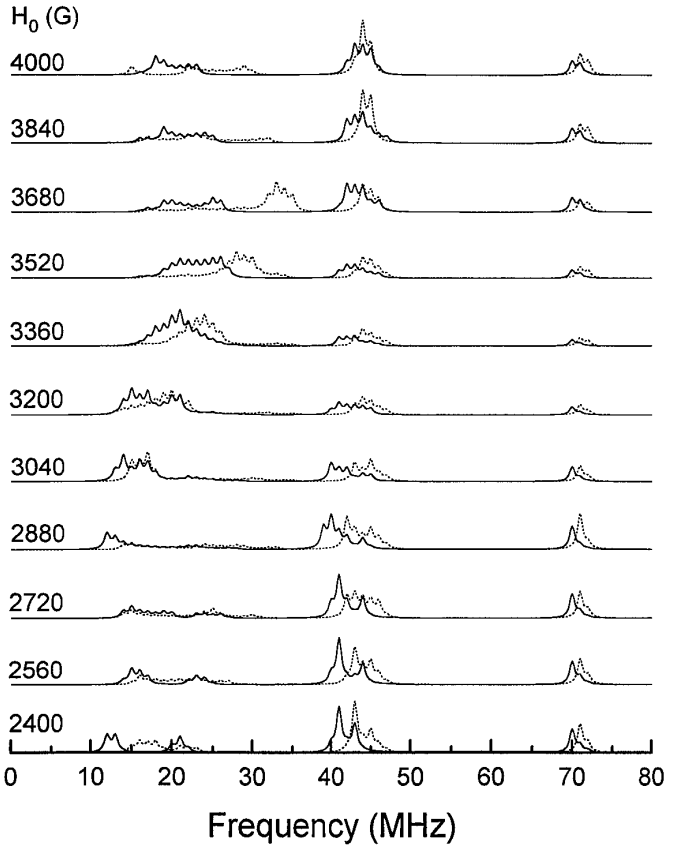

FIG. 9. Simulated orientation-selective ENDOR spectra calculated with $a_{iso} = -28.8$ MHz, $D = 1500$ MHz, $\eta = 0.2$, $\Delta H = 15$ G, and $\Delta\nu = 0.1$ GHz. Spectra obtained using the exact calculation appear in solid lines, whereas those obtained using the perturbation method are represented by dotted lines.

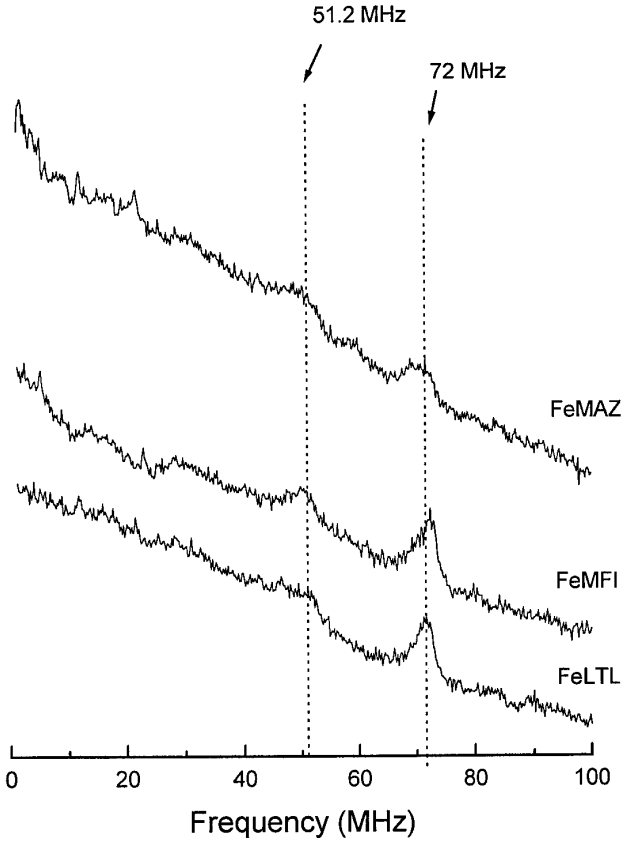

FIG. 10. Davies ENDOR spectra of ^{57}Fe MAZ (H_0 = 5000 G), ^{57}Fe MFI (H_0 = 5311 G), and ^{57}Fe LTL (H_0 = 5000 G). For all spectra, t_{RF} = 2.0 μs, and τ = 0.34 μs except for ^{57}Fe LTL where τ = 0.23 μs.

ZFS interaction, particularly on the asymmetry parameter η. Furthermore, when the experiments are carried out at very low temperature ($<$2K), the sign of a_{iso} can be determined from the relative intensities of the components of the $\nu_{\pm 5/2}$ doublet. When $\eta < \frac{1}{3}$, it is also possible to determine the sign of D by comparing the relative intensities within the $\nu_{\pm 5/2}$ doublet at the lower and upper field edges of the EPR spectrum.

The theoretical analysis of the spectra show that a_{iso} is best determined from the $\nu_{\pm 5/2}$ doublet which is the least dependent on the ZFS interaction. Hence, the appearance of the $\nu_{\pm 5/2}$ doublet at 72 MHz for ^{57}FeLTL, ^{57}FeMFI, and ^{57}FeMAZ indicates that their a_{iso} values are similar to that of ^{57}FeSOD (-28.8 MHz). Therefore, a a_{iso} value of -29 MHz can be considered as a typical value for ^{57}Fe in a zeolite framework site. A more detailed discussion of this value as compared to other oxides was given in our recent high-field ENDOR work (*23*).

In the particular case of ^{57}Fe(III) ($S = \frac{5}{2}$), the observation of the inhomogeneous contributions of the ZFS were easily identified since the hyperfine coupling is primarily isotropic. The same is expected for $^{55}Mn^{2+}$. However, the hyperfine interactions with ligand nuclei are expected to be anisotropic, and the separation of the two effects is more complex. In this case, the analysis would require a predetermination of D and E from the EPR spectrum.

When the hyperfine coupling is small, the effective nuclear Hamiltonian approach becomes valid and can be used for the analysis of the spectrum. In this case, however, the inhomogeneous broadening introduced by the ZFS is small and probably negligible as it depends on terms of the form $a_{iso}D^2/\nu_0^2$. Indeed the ^1H pulsed and CW ENDOR spectra of $Mn(H_2O)_6^{+2}$ in a frozen solution could be well simulated without taking the ZFS into account (D = 555 MHz) (*32*). The third approach should be also valid for simulations of ESEEM spectra where small hyperfine couplings are involved. This would require the calculation of the eigenvectors of the nuclear Hamiltonians given in Eq. [13], and then the general expressions of Mims can be used (*34, 36*). For ESEEM, it has been shown that the modulation depth, rather than the modulation frequency is sensitive to D (*36*).

When D becomes much greater than the electronic Zeeman interaction ($g\beta H_0 \ll D$), the ENDOR spectral characteristics of high spin ^{57}Fe(III) are significantly different than those discussed in this work. In this case, the ZFS term is taken as the zeroth-order Hamiltonian; the electronic Zeeman and hyperfine terms are treated as perturbations, and the ground state can be treated as an effective $S = \frac{1}{2}$ with an effective g value (*39*). The ENDOR spectrum of such a system consists of a doublet, the position of which depends on the hyperfine coupling and the effective g values. The splitting of the doublet is determined by the so-called pseudonuclear Zeeman effect. The latter introduces an anisotropy into the spectrum which is determined by the orientation of the ZFS tensor with respect to the external magnetic field (*39–41*).

CONCLUSIONS

X-band ENDOR spectra of high-spin ^{57}Fe(III)-substituted sodalite exhibited three doublets which are orientation dependent in terms of both frequencies and relative intensities. This orientation dependence was attributed to the ZFS interaction, and a theoretical treatment showed that the effect can be accounted for, using third-order perturbation theory up to $D < 500$ MHz. The isotropic hyperfine interaction is best determined from the ENDOR frequencies within the $M_s = \pm 5/2$ manifolds which are the least sensitive to the ZFS. If only these ENDOR frequencies are considered, third-order perturbation expressions are valid if $D < 1000$ MHz.

APPENDIX A

The perturbation Hamiltonian, H', consists of the ZFS interaction only

$$H' = A[\hat{S}_z^2 - \tfrac{1}{3}S(S+1)] + B_+(\hat{S}_+\hat{S}_z + \hat{S}_z\hat{S}_+) + B_-(\hat{S}_-\hat{S}_z + \hat{S}_z\hat{S}_-) + C_+\hat{S}_+^2 + C_-\hat{S}_-^2, \quad [18]$$

and the eigenvectors, corrected to second order, are

$$|i\rangle = |i\rangle^{(0)} + |i\rangle^{(1)} + |i\rangle^{(2)},$$

where the number in parentheses corresponds to the order of the correction. Using standard nondegenerate perturbation theory (*42*), $|i\rangle$ is given by

$$|i\rangle = |i\rangle^{(0)} + \sum_{j\neq i}\frac{H'_{j,i}}{\omega_i - \omega_j}|j\rangle^{(0)} + \sum_{k\neq i}\sum_{j\neq i}\frac{H'_{k,j}H'_{j,i}}{(\omega_i-\omega_j)(\omega_i-\omega_k)} - \frac{H'_{i,i}H'_{k,i}}{(\omega_i-\omega_k)^2}|k\rangle^{(0)}.$$

The expectation values $\langle S'_z\rangle_{M_S}$ then become

$$\begin{aligned}\langle S'_z\rangle_{M_{S,i}} &= \langle i|S_z|i\rangle \\ &= M_{S,i} + \sum_{j\neq i}\left|\frac{H'_{j,i}}{\omega_i-\omega_j}\right|^2 M_{S,j} + \sum_{k\neq i}\left|\sum_{j\neq i}\times\frac{H'_{k,j}H'_{j,i}}{(\omega_i-\omega_j)(\omega_i-\omega_k)} - \frac{H'_{i,i}H'_{k,i}}{(\omega_i-\omega_k)^2}\right|^2 M_{S,k} \\ &\quad + \sum_{j\neq i}\left(\frac{H'_{j,i}}{\omega_i-\omega_j}\right)^*\sum_{l\neq i}\left(\frac{H'_{j,l}H'_{l,i}}{(\omega_i-\omega_l)(\omega_i-\omega_j)} - \frac{H'_{i,i}H'_{j,i}}{(\omega_i-\omega_j)^2}\right)M_{S,j} + \sum_{j\neq i}\left(\frac{H'_{j,i}}{\omega_i-\omega_j}\right)\sum_{l\neq i}\times\left(\frac{H'_{j,l}H'_{l,i}}{(\omega_i-\omega_l)(\omega_i-\omega_j)} - \frac{H'_{i,i}H'_{j,i}}{(\omega_i-\omega_j)^2}\right)^* M_{S,j}.\end{aligned}$$

ACKNOWLEDGMENT

This research was supported by a grant from the United States–Israel Binational Science Foundation (BSF), Jerusalem, Israel.

REFERENCES

1. G. Zi, T. Dake, and Z. Ruiming, *Zeolites* **8,** 453 (1988).
2. A. N. Kotasthane, V. P. Shiralkar, S. G. Hegde, and S. B. Kulkarni, *Zeolites* **6,** 253 (1986).
3. T. Inui, H. Nagata, T. Takeguchi, S. Iwamato, H. Matsuda, and M. Inoue, *J. Catal.* **139,** 482 (1993).
4. D. H. Lin, G. Coudurier, J. Vedrine, *in* ''Zeolites: Facts, Figures, Future'' (P. A. Jacobs, and R. A. van Santen, Eds.), p. 1431, Elsevier, Amsterdam, 1989.
5. J. Patarin, M. Tuilier, J. Durr, and H. Kessler, *Zeolites* **12,** 70 (1992).
6. I. J. Pickering, D. E. W. Vaughan, K. G. Strohmaier, G. N. George, and G. H. Via, *in* ''Proceedings of the 9th International Zeolite Conference'' (R. von Ballmoos, M. M. J. Treacy, and J. B. Higgins, Eds.), p. 197, Butterworth/Heinemann, Stoneham, Massachusetts, 1993.
7. D. E. W. Vaughan, K. G. Strohmaier, I. J. Pickering, and G. N. Goerge, *Solid State Ionics* **53–56,** 1282 (1992).
8. S. A. Axon, K. K. Fox, S. W. Carr, and J. Klinowski, *Chem. Phys. Lett.* **189,** 1 (1992).
9. S. Bordiga, R. Buzzoni, F. Geobaldo, C. Lamberti, E. Giamello, A. Zecchina, G. Leofanti, G. Petrini, G. Tozzola, and G. Vlaic, *J. Catal.* **158,** 486 (1996), and references therein.
10. B. D. McNicole and G. T. Pott, *J. Catal.* **25,** 169 (1972).
11. G. T. Derouane, M. Mestdagh, and I. J. Vielvoye, *J. Catal.* **33,** 169 (1974).
12. P. Ratnasami and R. Kumar, *Catal. Today* **9,** 328 (1991).
13. D. Goldfarb, M. Bernardo, K. G. Strohmaier, D. E. W. Vaughan, and H. Thomann, *J. Am. Chem. Soc.* **116,** 6344 (1994).
14. C. Gemperle and A. Schweiger, *Chem. Rev.* **91,** 1481 (1991).
15. H. Kurreck, B. Kirste, and W. Lubitz, ''Electron Nuclear Double resonance Spectroscopy of radicals in Solution,'' VCH, Weinheim/New York, 1988.
16. L. Kevan, *in* ''Time Domain Electron Spin Resonance'' (L. Kevan and R. N. Schwartz, Eds.), p. 279, Wiley, New York, 1979.
17. S. A. Dikanov and Yu. D. Tsevetkov, ''Electron Spin Echo Envelope Modulation (ESEEM) Spectroscopy,'' CRC Press, Boaca Raton, Florida, 1992.
18. J. C. M. Henning, *Phys. Lett. A* **24,** 40 (1967).
19. B. E. Sturgeon, J. A. Ball, D. W. Randall, and R. D. Britt, *J. Phys. Chem.* **98,** 1287 (1994).
20. P. R. Locher and S. Geschwind, *Phys. Rev. A* **139,** 991 (1965).
21. J. R. Brisson and A. Manoogian, *Phys. Rev. B* **18,** 4576 (1978).
22. W. Rhein, *Z. Naturforsch.* **27,** 741 (1972).
23. D. Goldfarb, K. G. Strohmaier, D. E. W. Vaughan, H. Thomann, O. G. Poluektov, and J. Schmidt, *J. Am. Chem. Soc.* **118,** 4665 (1996).
24. D. E. W. Vaughan and K. G. Strohmaier, U.S. Patent 5,185,136 (1993).
25. H. W. Kouwenhoven and W. H. Stork, U.S. Patent 4,208,305 (1980).
26. H. Thomann and M. Bernardo, *Spectrosc. Int. J.* **8,** 119 (1990).
27. H. Thomann and M. Bernardo, *in* ''Metallobiochemistry Part D'' (J. Riordan and B. L. Vallee, Eds.), Vol. 227, p. 118, Academic Press, San Diego, 1993.
28. E. R. Davies, *Phys. Lett. A* **47,** 1 (1973).
29. H. Thomann and M. Bernardo, *Chem. Phys. Lett.* **169,** 5 (1990).
30. M. Mehring, P. Höfer, and A. Grupp, *Ber. Bunsenges. Phys. Chem.* **91,** 1132 (1987).
31. D. Goldfarb, M. Bernardo, K. G. Strohmaier, D. E. W. Vaughan, and H. Thoamann, *in* ''Zeolites and Related Microporous Materials, State of the Art 1994'' (J. Weitkamp, H. G. Karger, H. Pfiefer, and

W. Holderich, Eds.), Studies in Surface Science and Catalysis, Vol. 84, p. 403, (1994).

32. X. Tan, M. Bernardo, H. Thomann, and C. P. Scholes, *J. Chem. Phys.* **98,** 5147 (1993).

33. E. Meirovitch and R. Poupko, *J. Phys. Chem.* **82,** 1920 (1978).

34. W. B. Mims, *Phys. Rev. B* **5,** 2409 (1972).

35. R. G. Larsen, C. J. Halkides, and D. J. Singel, *J. Chem. Phys.* **98,** 6784 (1993).

36. A. Coffino and J. Peisach, *J. Chem. Phys.* **97,** 3072 (1992).

37. B. J. Gaffney and H. J. Silverstone, *Biol. Magn. Reson.* **13,** 1 (1993).

38. R. Vardi and D. Goldfarb, unpublished results.

39. A. Abragam and B. Bleaney, ''Electron Paramagnetic resonance of Transition Ions,'' Clarendon Press, Oxford 1970.

40. C. P. Scholes, R. A. Isaacson, T. Yonetani, and G. Feher, *Biochem. Biophys. Acta* **322,** 457 (1973).

41. G. A. Rottman, K. Doi, O. Zak, R. Aasa, and P. Aisen, *J. Am. Chem. Soc.* **111,** 8613 (1989).

42. J. P. Lowe, ''Quantum Chemistry,'' second ed., Academic Press, San Diego, 1993.